*Nigerian Research Journal of Chemical Sciences* (ISSN: 2682-6054)
Volume 13, Issue 2, 2025

# Synthesis and effect of annealing temperature on the structural, magnetic and photocatalytic properties of $Gd_{0.5}Bi_{0.3}Ca_{0.2}Fe_{0.5}In_{0.5}O_{3-\delta}$

*Ibrahim Abdulkadir, Salisu Abubakar and Abdurrashid Haruna

Department of Chemistry,

Ahmadu Bello University, Zaria, Kaduna State, Nigeria.

*Corresponding Author: Ibrahim.abdulkadir@gmail.com

***Accepted: September 23, 2025. Published Online: September 29, 2025***

## ABSTRACT

Novel perovskite-type nanomaterials with the composition $Gd_{0.5}Bi_{0.3}Ca_{0.2}Fe_{0.5}In_{0.5}O_{3-\delta}$ were synthesized by using the citric acid route. The powders were calcined and annealed at temperatures from 400 to 900 °C, and characterized using scanning electron microscopy (SEM), and transmission electron microscopy, powder X-ray diffraction analysis (PXRD), Brauner Emmett and Teller (BET), and a Vibrating sample magnetometer (VSM), while the powders were screened for photocatalytic activity against an organic dye using FTIR. The results showed that the powders contain crystalline nanoparticles and the crystalline sizes increased with increase in annealing temperature ($T_A$). PXRD analysis indicated that the powders crystallized in an orthorhombic lattice structure with space group *pbnm*. The BET specific surface areas (SSA) for the powders ranged between 2.76-27.37 $m^2 g^{-1}$, showing a decrease in surface area as $T_A$ increased, with an activation energy of 20 kJ $mol^{-1}$. VSM analysis of the hysteresis loop showed a continuous slight increase in coercive field (39-268 Oe) with increasing annealing temperature and a rapid reduction in saturation magnitization *Ms* values (from 9.0 to 1.1 emu $g^{-1}$). Values obtained for powder efficiency are 59.47, 78.88 and 85.53 % for powders annealed at 700, 800 and 900 °C respectively. These materials showed good potential for the photocatalytic degradation of organic pollutants.

**Keywords**: Perovskites, magnetic properties, coercive field, photocatalytic activities, Ca doped.

## INTRODUCTION

One outstanding family of materials that have received considerable attention are the perovskites and the perovskite-like materials. These are a group of materials that can generally be represented by the formula $ABX_3$ (where $A^{3+}$ could be a large rare-earth metal, $B^{3+}$ is a smaller transition metal and $X^{2-}$ is a nonmetal, mostly, oxygen). They have a tendency for displaying interesting

characteristics due to the flexibility of these compounds and their ability to accommodate almost all the elements on the periodic table in different types of combinations.

Perovskite-like materials have found use in several fields of advanced technologies such as gas sensors [1-4], electric and magnetic materials [5-8], solid oxide fuel cells [9, 10], catalysis and photocatalysis [11-13]. The fascinating properties of this group of materials stems from the chemistry of the perovskite structure ($ABO_3$), which is flexible and allows for substitution and/or replacement of the ions on either of the sites (A or B-site) in a variety of combinations.

The orthoferrites are members of the perovskite family in which the A-site is occupied by a rare earth metal and the B site by a smaller transition metal. They also display properties such as ferromagnetic and ferroelectric, pyro and piezoelectric [14-16], catalytic as well as photocatalytic properties [17-20].

Materials with novel properties can be made by introducing (doping or partial substitution on the A and/or B sites) ions with varied physical properties of interest into the lattice of the perovskite structure to impart on the material the required properties [21, 22]. The change in properties of doped perovskites can also arise from a change in the bond lengths in the lattice, creation of defects in the lattice or creation of oxygen deficiency, and metals with smaller ionic sizes ($Ca^{2+}$, $Sr^{2+}$ and $Ba^{2+}$) have been used for this purpose [23-26].

In this work, a simple citric acid route is used to synthesize a novel perovskite-like material $Gd_{0.5}Bi_{0.3}Ca_{0.2}Fe_{0.5}In_{0.5}O_{3-\delta}$ and the effect of annealing temperature on the structural and magnetic properties was analysed. The Pechini synthesis method is a useful technique for fabricating metal oxides, employing chelating agents like citric acid and ethylene glycol to form a homogeneous metal-citrate complex solution [27]. Also, the effect of annealing temperature on the photocatalytic properties of the powders on the degradation of rhodamine B (RhB) dye was studied.

## MATERIALS AND METHODS

### *Materials*

The following precursor chemicals where used as obtained; $Fe(NO_3).9H_2O$ (98%) (Saarchem), $Gd(NO_3)_3$ (99.8%) (BDH Chemicals), $In(NO_3)_3$ $Bi(NO_3)_3.5H_2O$ (97%) (Saarchem), $Ca(NO_3)_2$ (99%) (Saarchem), $K_2Cr_2O_7$ (99%) $Ag_2SO_4$ (99%) (Saarchem), citric acid (99.7%) (BDH Chemicals). Also used were analytical grade concentrated $H_2SO_4$ (98%), $HgSO_4$ (99%) and $(NH_4)_2Fe(SO_4)_2.6H_2O$

(99%) (Merck), concentrated HCl (37%) and $HNO_3$ (55%) (Promark Reagents), ethylene glycol (99%) (Promark Chemicals).

Rhodamine B, and $H_2O_2$ 30% vol. (100 vol) (Minema Chemicals) were used as received to conduct the photocatalytic screening.

Deionized water from a Millipore Milli-Q Elix 5 UV water purification system was used throughout this work.

***Synthesis of* $Gd_{0.5}Bi_{0.3}Ca_{0.2}Fe_{0.5}In_{0.5}O_{3-\delta}$**

$Gd_{0.5}Bi_{0.3}Ca_{0.2}Fe_{0.5}In_{0.5}O_{3-\delta}$ sample was prepared by a citric acid sol-gel process [28]. $Fe(NO_3).9H_2O$ (0.015 mol) was dissolved in deionized water (20.00 $cm^{-3}$). $Gd(NO_3)_3.6H_2O$ (0.015 mol), $Ca(NO_3)_2$ (0.006 mol), $In(NO_3)_3.5H_2O$ (0.015mol) and $Bi(NO_3)_3.5H_2O$ (0.009 mol) were dissolved in dilute nitric acid (about 15 $cm^3$, 6 mol $dm^{-3}$) solution to give the amount of metals required to fulfil the material's stoichiometry. The two solutions were mixed thoroughly, made up to 200 $cm^3$ with deionized water and then gradually poured into a burette. The solution was then added (drop-wise) to a citric acid solution (400 $cm^3$, 0.15 mol) in a beaker which was continuously stirred by magnetic stirrer at room temperature to form a clear solution. Once the addition was completed and still stirring, the temperature of the mixture was raised to 90 $^oC$ and allowed to stand until the volume of the solution was reduced to about 50 $cm^3$, ethylene glycol (100 $cm^3$) was added and the heating and stirring continued until a thick gel was formed. The gel was then removed from the beaker and placed in a crucible in an oven at a temperature of 120 $^oC$ for 24 h to dry. The dry gel was subsequently pre-calcined at 400 $^oC$ for 4 h to remove all the organic components. Separate sample portions of the precalcined dry gel were subsequently annealed in a muffle furnace for 4 h at annealing temperatures ($T_A$) of 500, 600, 700, 800 and 900 $^oC$ respectively.

***Characterisation***

Transmission electron microscopy micrographs were collected on a JEOL JEM 1010 instrument. Also, scanning electron microscopy data were collected on a ZEISS Ultra plus field emission gun scanning electron microscope for the analysis of the morphology of the crystals. The crystals lattice structures were determined by powder X-ray diffraction (PXRD) analysis by using a Bruker Advance D8 diffractometer equipped with a Cu $K_\alpha$ radiation source.

Crystallite sizes (D) were calculated by using the Scherrer equation (1),

$$D = k\lambda/\beta\cos\theta \quad (1)$$

(where k is the Scherrer constant, λ is the wavelength of the radiation and β is the full width at half maximum).

Specific surface areas and pore sizes were determined by nitrogen adsorption and the BET equation method with a Micromeritrics Tristar II 3020 fully automated three station surface area and porosity analyzer.

The magnetic properties were analysed by using a LakeShore model 735 vibrating sample magnetometer. The maximum applied magnetic field was 14 kOe and analyses were done at room temperature.

The thermal stability of the powders was analysed on a thermogravimetric analysis (TGA) and differential scanning calorimetry (DSC) instrument (TA Instruments SDT-Q600 thermal analyzer). Data was collected in air (during combustion) for the sample between 25 and 1000 °C.

Surface characterization of the powders was carried out on a Perkin Elmer FTIR Spectrum 100 spectrometer fitted with an attenuated total reflectance (ATR) accessory.

***Photocatalytic screening***

The photocatalytic activity of each sample was tested on Rhodamine B dye in the presence of $H_2O_2$ at room temperature [29]. A 26 W fluorescent lamp (Osram Dulux D, 26 W, 1800 lm) placed in a quartz jacket and held at about 7 cm above the RhB dye solution (which was continuously being stirred with a magnetic stirrer) was used for the irradiation. The system contained 1.5 g $dm^{-3}$ of synthesized materials and $H_2O_2$ ($3.0 \times 10^{-5}$ mol $dm^{-3}$). A period of 30 min was allowed for equilibration in the dark before the lamp was turned on. Aliquots of the dye solution where withdrawn at intervals of 20 min to monitor the photodegradation process by measuring the absorbance of the withdrawn aliquot at a $\lambda_{max}$ of 556 nm on a Biochrom Libra S6 UV spectrophotometer. The extent of mineralization was also investigated by determining the chemical oxygen demand (COD) of the degraded solution after 180 min of degradation activity by mean of standard method as described in the literature [30-31].

## RESULTS AND DISCUSSION

A dry dark brown powder of the material $Gd_{0.5}Bi_{0.3}Ca_{0.2}Fe_{0.5}In_{0.5}O_{3-\delta}$ was obtained after the precalcination process. The colour of the powders changed gradually from brown to black with increasing annealing temperature. Six samples were obtained in all. The samples were tagged

GdCaI followed by the number indicating the annealing temperature, $T_A$, at which each powder was annealed (GdCaI400, GdCaI500 and GdCaI600 for samples annealed at 400, 500 and 600 °C respectively).

***Crystal phase characterization***

The PXRD diffractograms for the samples prepared at annealing temperatures ($T_A$) of 400-900 °C are shown in Figure 1. The perovskite peaks are seen growing at $T_A$ 400 °C, indicating that the nucleation and growth of the perovskite phase begins at a lower temperature. Peaks corresponding to the 100, 110, 111, 200, 210 and 211 perovskite planes were identified in the diffractogram at $T_A$ 400 °C. Prominent peaks belonging to other lattice structures indicate that at 400 °C, the powder contains largely mixed oxides and probably some amorphous materials. The perovskite peak intensities increase at higher $T_A$ while the non perovskite peaks disappeared, indicating an increase in crystallinity and also an increase in the phase purity of the perovskite phase.

The powders crystallized in a pure orthorhombic perovskite phase of space group *Pbnm* at higher $T_A$ (600 °C and above). The absence of impurity peaks indicates that the ions have all been incorporated into the perovskite lattice. The peak broadening at 600 and 700 °C annealing temperatures is due to the nanoparticulate nature of the particles. A slight reduction in the broadening of the peaks at higher $T_A$ indicates an increase in crystallite sizes which is confirmed by the SEM and TEM micrographs and also by the crystallite size values obtained by applying the Scherrer equation to the 110 peak (Table 1). Higher $T_A$, therefore, are accompanied by an increase in phase purity, crystallinity as well as crystallite sizes.

The calculated lattice parameters obtained by matching samples peaks to that of $(Gd_{0.4}Sr_{0.6})FeO_3$ (PDF 01-082-1963) are presented in Table 1. A slight decrease is observed in the cell volume between $T_A$ 500 and 600 °C. This could be attributed to a stabilization of higher oxidation states for the transition metals which will lead to a decrease in the ionic sizes ($Fe^{4+}$ is smaller in size than $Fe^{3+}$) of the ions. A sudden increase in cell volume is noticed at $T_A$ 700 °C. This could be the point at which the ions are maximally incorporated into the perovskite lattice. The decrease in the cell volume which is observed afterwards may be as a result of phase separation.

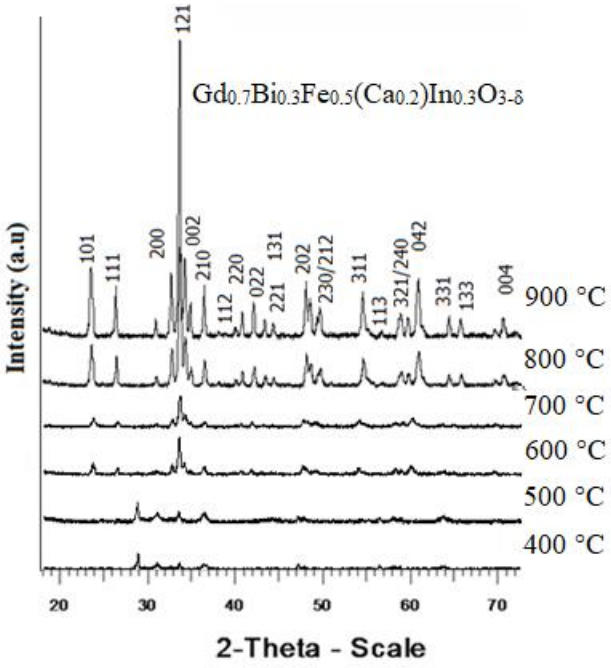


Figure 1: Powder X-ray diffractograms for the powders showing the evolution of the perovskite peaks as the annealing temperatures increased from 400 to 900 °C.

Table 1: Variation in cell parameters and crystallite sizes for entire temperature range

| Samples | Cell parameters | | | | Space group | Lattice system | $R/R_0$ | Crystallite sizes |
|---|---|---|---|---|---|---|---|---|
| | a /Å | b /Å | c /Å | V /Å | | | | Nm |
| GdCa400 | | | | | | | | 15.985 |
| GdCa500 | 5.2800 | 5.5100 | 7.6854 | 405.45 | *Pbnm* | Orthorhombic | 9.52 | 16.523 |
| GdCa600 | 5.3149 | 5.5049 | 7.7046 | 404.46 | *Pbnm* | Orthorhombic | 9.55 | 17.686 |
| GdCa700 | 5.3284 | 5.5284 | 7.7145 | 410.94 | *Pbnm* | Orthorhombic | 8.51 | 22.345 |
| GdCa800 | 5.3374 | 5.5074 | 7.7328 | 407.29 | *Pbnm* | Orthorhombic | 9.28 | 31.837 |
| GdCa900 | 5.3498 | 5.5018 | 7.7450 | 405.93 | *Pbnm* | Orthorhombic | 9.04 | 37.911 |

***Morphology***

Figure 2 shows the TEM micrographs for samples GdCaI400, GdCaI600, GdCaI700 and GdCaI900. The sample annealed at 400 °C shows crystals at the nucleation stage among other undifferentiated amorphous substances (Figure 2 (a)). This implies that the duration of the calcination (4 h) is long

enough for the crystals to begin to nucleate. At 600 and 700 °C, the crystals have grown in size and are more spherical in shape (Figure 2 (b and c)). The crystallite sizes observed at this stage range between 17 to 25 nm. At 900 °C the crystals become even bigger and opaque due to increased density (Figure 2 (d)). At this stage the powder consists more of large aggregates of crystals with widely varied crystal sizes (Figure 2 (c)).

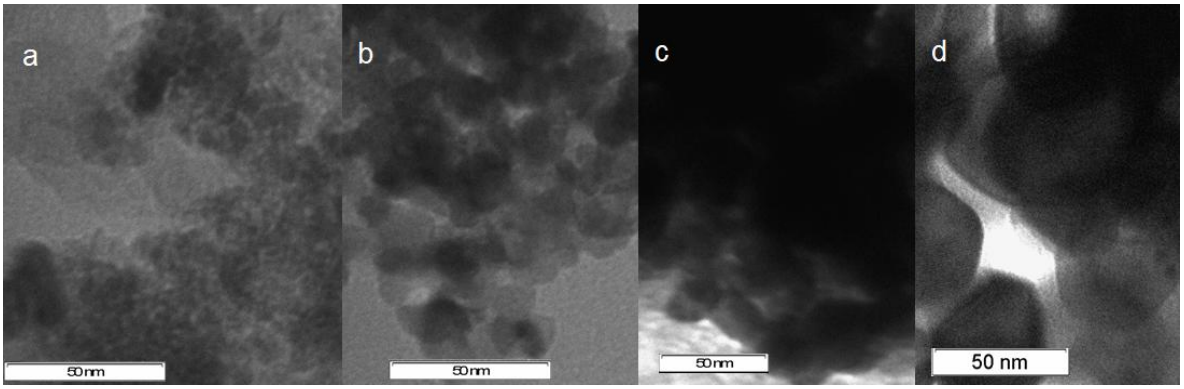


Figure 2: TEM images for (a) GdCa400, GdCaI600, (c) GdCa700 and (d) GdCa900 showing the increase in crystallite size as $T_A$ increases.

Figure 3(a-d) displays SEM micrographs of crystals of GdCaI400, GdCaI600, GdCaI700 and GdCaI900 respectively. The increase in crystallite sizes and the clustering of the crystals can be seen clearly.

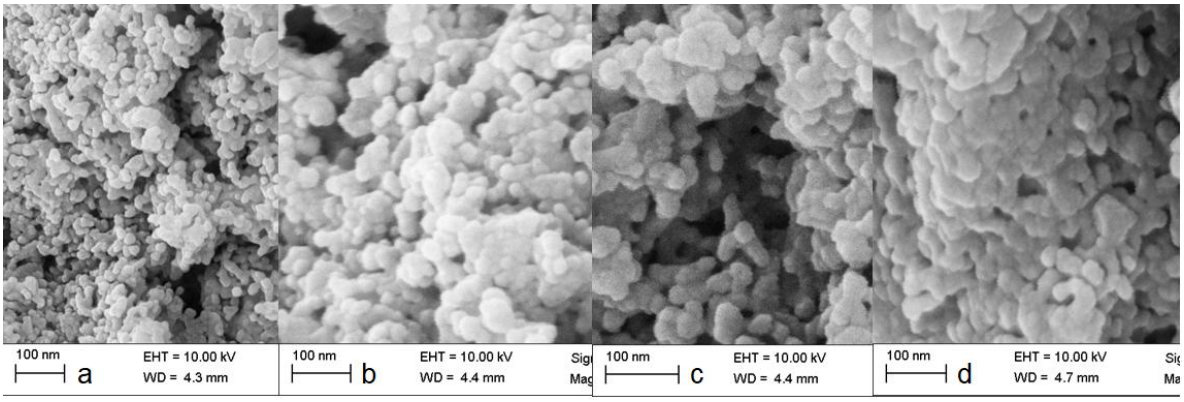


Figure 3: Scanning electron microscopy micrographs for (a) GdCaI400, (b) GdCaI600, (c) GdCaI700 and (c) GdCaI900.

***BET surface area***

The nitrogen adsorption-desorption isotherms for the powders are presented in Figure 4.

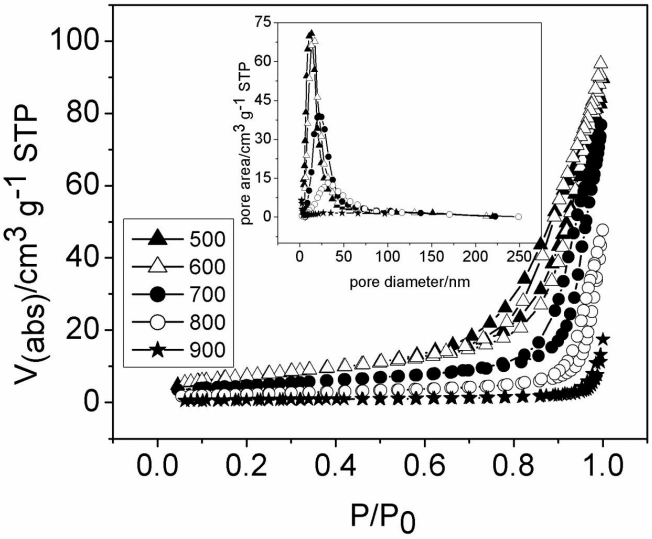


Figure 4: Adsorption-desorption isotherms for GdCaI500-900.

The hysteresis loop moves towards higher relative pressure as the annealing temperature increases. The inset show plots of the pore size distribution for GdCaI500-900 showing the decrease in the mesoporous peak area as the annealing temperature increases.

The isotherms correspond to the type II isotherm on the IUPAC scale [32]. The BET specific surface areas (SSA) range is between 3.68-34.8 $m^2$ $g^{-1}$ (Table 2) and display an inverse relationship between SSA and $T_A$. As $T_A$ increases, SSA decreases as shown in Figure 5.

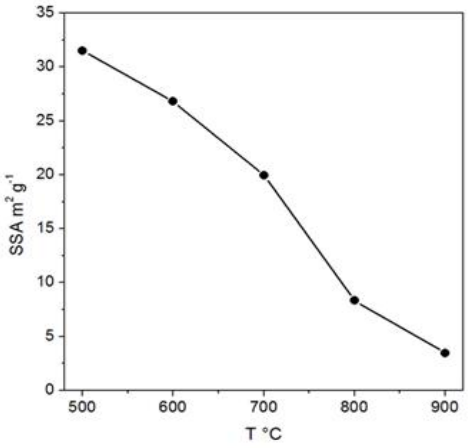


Figure 5: Decrease in specific surface area as annealing temperature increases.

The hysteresis loop is shrinking due to loss of mesopore area. This leads to significant loss in SSA and the value of $P/P_O$ is pushed much closer to 1 at higher $T_A$ indicating a preponderance of macropores at higher $T_A$. This is also seen from the pore size distribution in the inset in Figure 4. At $T_A$ 400 to 600 °C, the peak positions of the pores are mostly below 50 nm indicating the presence of mostly mesopores at low $T_A$ value. The sharp pore peaks also indicate a narrow pore size distribution range in the powders. As the $T_A$ increases, however, the pore area drops rapidly as the peak area drastically flattens out for powders annealed at higher $T_A$ and shifts towards larger pore sizes (above 50 nm) in agreement with the adsorption-desorption hysteresis loop until it finally disappears at $T_A$ 900 °C. The decrease in the mesopore areas, and the increase in particle sizes, is responsible for the overall decrease in the values of the specific surface areas of the powders.

Figure 6 shows the Arrhenius fit for the relationship between the natural log of the BET specific surface area ($\ln S_{BET}$) and the reciprocal of the $T_A$ ($K^{-1}$) given by equation 2.

$$ln\, S_{BET} = ln\, A - \frac{E_A}{R}(1|T) \qquad (2)$$

where $S_{BET}$ is the BET specific surface area, $E_A$ is the activation energy for surface reduction, $R$ is the universal gas constant (value 8.314 J $K^{-1}$ $mol^{-1}$), $T$ is the annealing temperature, and $A$ is a constant.

The calculated value for the $E_A$ from the slope of the graph is 20±2.8 kJ $mol^{-1}$. This value falls within the range of values reported for pure $LaFeO_3$ (between 20 [33] and 28 kJ $mol^{-1}$ [34]).

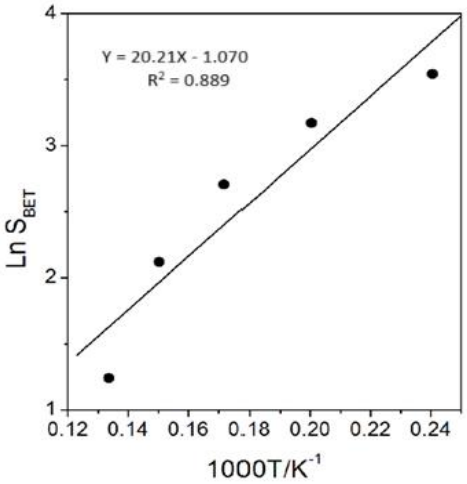


Figure 6: Arrhenius plot for GdCaI500-900 from which the activation energy for surface reduction was obtained.

***Surface characterization***

Figure 7 shows the Fourier transform infrared (FTIR) spectra of the samples measured between 380-4000 $cm^{-1}$.

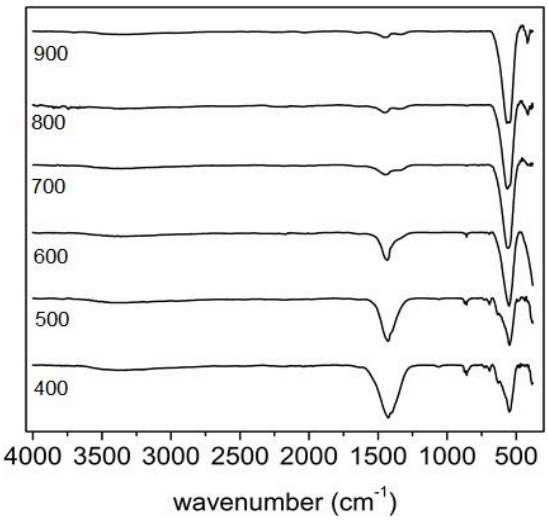


Figure 7: Fourier transform infrared spectra for GdCaI400-900 showing the reduction in peak intensity at 1400 $cm^{-1}$ and an increase in peak intensity at 600 $cm^{-1}$ with increase in annealing temperature.

The spectra show two important bands, one at about 1400 $cm^{-1}$ and the other at around 600 $cm^{-1}$. The band at 1400 $cm^{-1}$ is assigned to stretching vibrations of OH groups [35-36] either from M-OH species or from water molecules adsorbed on the surface of the crystals. Some have also attributed bands in this region to vibration ranges for varieties of carbonate species [37] or to the asymmetric and symmetric carbonyl group stretching vibration of ionized carboxylate [38]. The intensity of this band decreases as $T_A$ increases, indicating the removal of the water molecules, carbonates and carboxylates at the surface of the material. It could also be an indication of a reduction in surface area as $T_A$ increases. The band at 600 $cm^{-1}$ is assigned to stretching modes for O-Fe-O and other M-O bonds of the $BO_6$ octahedral units [39]. This is an indication of the progress of the formation of the perovskite lattice as was observed in the PXRD diffractograms.

***Thermal stability***

The results of TGA-DSC done on the precalcined powder (GdCaI400) are shown in Figure 8.

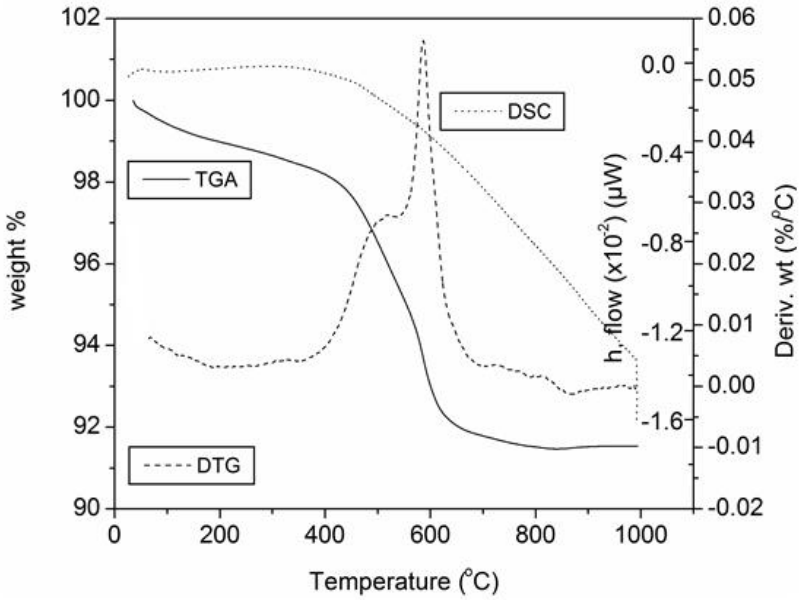


Figure 8: Thermal stability of the pre-calcined GdCaI400 powder between 25 and 1000 °C obtained in air.

The TGA shows thermal decomposition occurring in two different stages. The first stage, which involves the decomposition proceeding gradually between the range 25-380 °C, represents loss of small adsorbed molecules like $H_2O$ and $CO_2$ from combustion of surface bound organics [40]. The DSC within this temperature range shows that an endothermic process was involved. The sharp weight loss between 380-650 °C is attributed to the decomposition of oxalates to carbonates and the subsequent decomposition of the carbonate and other organic materials present. It is also accompanied by another DSC endothermic peak. The powder appears to stabilize thereafter with no further loss of weight. The crystallization process (which is exothermic) is unfortunately not captured on the DSC.

***Magnetic properties***

The result of the room temperature (RT) magnetization measurements of the powders is presented in Figure 9.

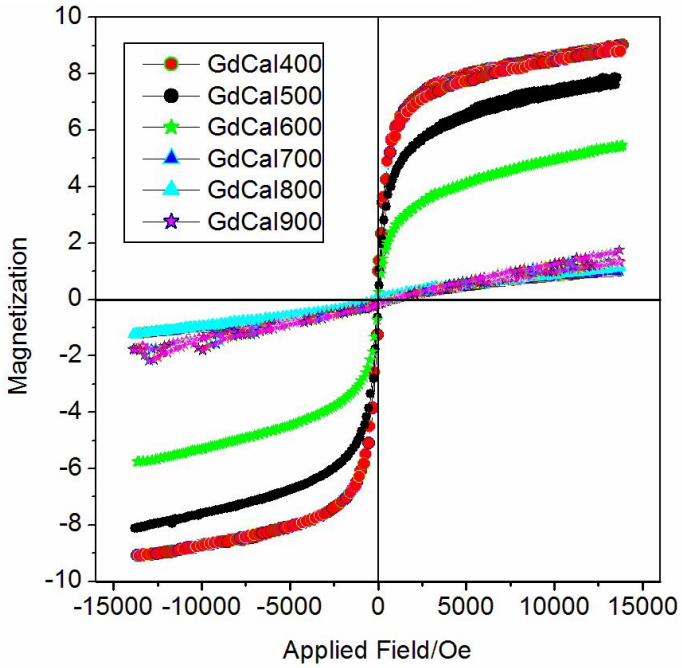


Figure 9: Magnetization hysteresis loops for (a) decreasing saturation magnetization for powders annealed at temperatures between 400 and 900 °C

The highest magnetization of 9.009 emu $g^{-1}$ was obtained for GdCaI400. A general decrease in magnetization is observed coupled with a gradual increase in the value of coercivity *Hc* as $T_A$ increases. This decrease in $M_S$ corresponds to the increase in crystallinity as can be seen from the PXRD (Figure 1).

Perovskites have been shown to have antiferromagnetic properties due to the formation of bond overlaps between Fe ions and the p orbitals of oxygen which leads to formation of $Fe^{3+}$-O-$M^{3+}$ bonds (where $M^{3+}$ is $Bi^{3+}$ or $Fe^{3+}$). The introduction of an $M^{2+}$ ion into the lattice would lead to a distortion in the bond angle of the Fe-O-Fe. Furthermore, the introduction of $M^{2+}$, in this case, $Ca^{2+}$ into the lattice would either lead to the formation of $Fe^{4+}$ in order to fulfil the requirements of charge compensation or result in the creation of oxygen vacancies and these contribute to the ferromagnetic characteristics [41-44]. As the perovskite lattice grows, more and more ions are incorporated into the crystal lattice and $Fe^{2+}$ ions are oxidized to $Fe^{3+}$ in the perovskite octahedral site. This leads to the formation of more of the antiferromagnetic $Fe^{3+}$-O-$M^{3+}$ superexchange which results in a reduction in the value of $M_S$ as $T_A$ increased. The reverse, however, is the case for values of the $H_C$. The $H_C$ values increased as $T_A$ increased (Table 2).

Table 2: Magnetization parameters for GdCaI400-900. Crystallite sizes were calculated from PXRD by using the Scherrer equation.

| Samples | $M_S$/emu $g^{-1}$ | $M_R$/emu $g^{-1}$ | $H_C$/Oe | $M_R/M_S$ | SSA/$m^2$ $g^{-1}$ |
|---|---|---|---|---|---|
| GdCaI400 | 9.0094 | 0.3949 | 39.056 | 0.044 | |
| GdCaI500 | 7.4453 | 0.3255 | 40.921 | 0.044 | 31.52 |
| GdCaI600 | 5.4660 | 0.0641 | 46.021 | 0.011 | 26.83 |
| GdCaI700 | 1.2839 | 0.0158 | 134.38 | 0.041 | 19.93 |
| GdCaI800 | 1.1110 | 0.0273 | 158.81 | 0.050 | 8.32 |
| GdCaI900 | 1.1949 | 0.0028 | 268.27 | 0.0452 | 3.45 |

Figure 10 shows the variation of $M_S$ and $H_C$ with $T_A$.

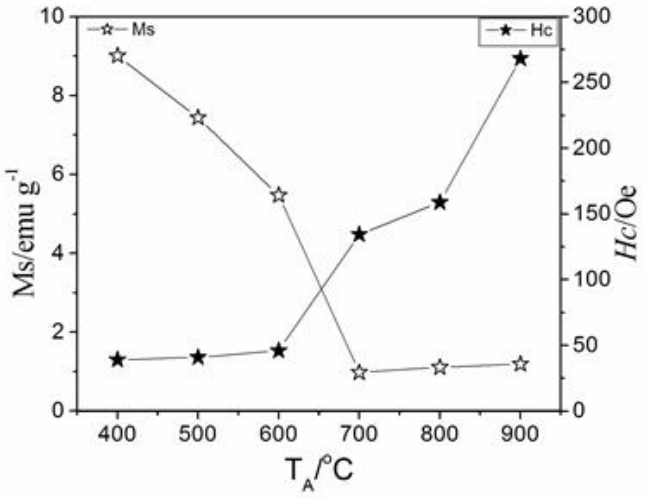


Figure 10: Variation of $M_S$ and $H_C$ with increasing $T_A$ for GdCaI400-900.

Only a slight increase in *Hc* is observed between $T_A$ 400 to 600 °C, the difference is more pronounced between $T_A$ 700 to 900 °C. For the *Ms* however, the drop is more pronounced at the lower $T_A$ (400 to 600 °C). The increase in $H_C$ can be attributed to the increase in sizes of the crystals and is related to the magnetocrystalline anisotropy [45], as the crystallite sizes increased with $T_A$. The squarness values ($M_R/M_s$) all remain low, indicating soft magnetic properties and do not show any discernible variation with the changing $T_A$.

***Photocatalytic screening***

The results of the photocatalytic screening of GdCaI400-900 on RhB dye are shown in Figure 11.

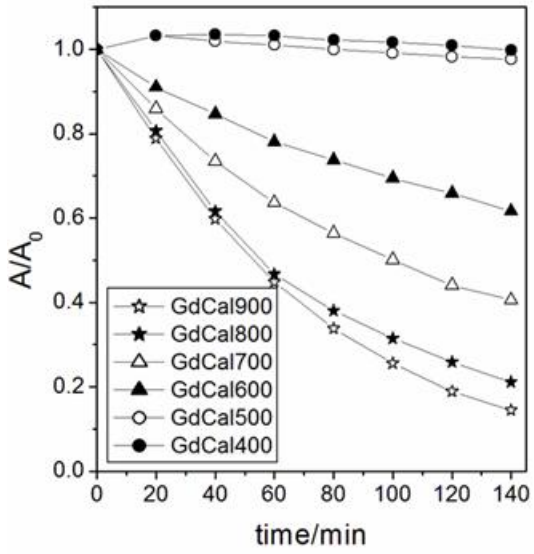


Figure 11: Photodegradation of RhB when irradiated with visible light for the photocatalysts GdCaI400-900 (1.5 g $dm^{-1}$) (a) in the absence of $H_2O_2$, and (b) in the presence of $H_2O_2$ ($3.0 \times 10^{-5}$ mol $dm^{-3}$).

The powders GdCaI600, GdCaI700, GdCaI800 and GdCaI900 all show significant photodegradation ability with the later three being the most active. The low or inactivity of powders annealed at lower $T_A$ (400-600 °C) may be due to the presence of some organic as well as amorphous materials blocking the dye molecules from reaching the surface of the powders. Powders annealed at higher $T_A$ (between 700 and 900 °C), however, do not have such barriers and therefore were able to degrade the dye solution faster.

Figure 12 shows the pseudo first-order kinetics of the photocatalytic processes and the values of the observed rate constants and the calculated percent efficiency (E/%) are shown in Table 3.

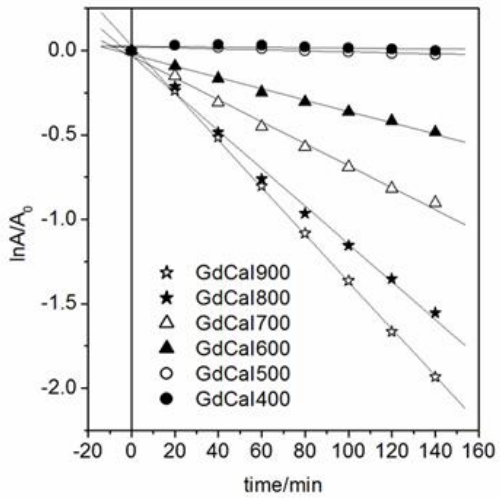


Figure 12: Pseudo-first-order rates for the degradation of RhB in the presence of 1.5 g $dm^{-3}$ of photocatalyst and 3.0 × $10^{-5}$ mol $dm^{-3}$ $H_2O_2$ after 140 min.

Table 3: Observed kinetics parameters for the photodegradation of RhB by 1.5 g $dm^{-3}$ of photocatalysts (GdCaI700-900) and 3.0 x $10^{-5}$ mol $dm^{-3}$ $H_2O_2$ after 140 min.

| Sample | $k_{obs}/min^{-1}$ | E/% |
|---|---|---|
| $H_2O_2$ | 4.4 × $10^{-6}$ | 0 |
| GdCaI400 | 1.0 × $10^{-4}$ | 0.14 |
| GdCaI500 | 3.0 × $10^{-4}$ | 2.32 |
| GdCaI600 | 3.4 × $10^{-3}$ | 38.39 |
| GdCaI700 | 6.5 × $10^{-3}$ | 59.47 |
| GdCaI800 | 1.12 × $10^{-2}$ | 78.88 |
| GdCaI900 | 1.4 × $10^{-2}$ | 85.53 |

The GdCaI700-900/$H_2O_2$ systems showed very high efficiency in decolourizing the test dye solution, indicating that the materials can act as excellent photocatalysts.

***Mineralisation of the RhB dye***

Table 4 shows the results for the chemical oxygen demand (COD) analysis of the dye solution over a period of 180 min of photodegradation activity in the presence of the powders (1.5 g $dm^{-1}$of each) and three drops of $H_2O_2$ (3.0 × $10^{-5}$ mol $dm^{-3}$).

Table 4: COD after 3 h of photodegradation of RhB dye for 1.5 $gdm^{-1}$ of GdCaI700, GdCaI800 and GdCaI900 in the presence of $H_2O_2$

| Sample | COD (mg $dm^{-3}$) | | | | E % |
|---|---|---|---|---|---|
| | 0 h | 1 h | 2 h | 3 h | At 3 h |
| GdCaI700 | 123 | 59 | 42 | 36.9 | 70 |
| GdCaI800 | 123 | 53 | 38 | 24.6 | 80 |
| GdCaI900 | 123 | 51 | 34 | 22.1 | 82 |

The consistent drop in the value of COD for all the samples every hour is evidence of continuous mineralization by the powders. The COD values obtained after three hours represent an efficiency of 70, 80 and 82 % for GdCaI700, GdCaI800 and GdCaI900 mineralisation of the organic dye respectively. This shows that the powders can be used to effectively degrade organic pollutants and convert them into harmless substances like $CO_2$ and $H_2O$.

## CONCLUSIONS

Perovskite-like $Gd_{0.5}Bi_{0.3}Ca_{0.2}Fe_{0.5}In_{0.5}O_{3-\delta}$ powders of crystallite size range 15.98 to 37.91 nm were synthesized via a simple citric acid route. The PXRD results show that the powders crystallized in a rhombohedral lattice with crystallite sizes increasing at higher $T_A$. The BET specific surface areas decreased with increase in $T_A$. The activation energy for the reduction of the material surface calculated from the Arrhenius plot is 41 kJ $mol^{-1}$. The saturation magnetization decreased gradually as $T_A$ increased. The powders annealed at 700, 800 and 900 °C showed marked photocatalytic activities for RhB degradation in the presence of $H_2O_2$ and more than to 85% decolourization of RhB was achieved for GdCaI900 and 82% mineralization after 3 hours of exposure to visible light. We recommend this material for use in degrading toxic organic dyes and pharmaceutical waste. They are easy to prepare and are capable of achieving a higher degree of mineralization of organic molecules

## Acknowledgement

IA is grateful to the Ahmadu Bello University and the Tertiary Education Trust Fund TETFUND for the award of an IBR research grant (TETF/DR&D/UNI/ZARIA/IBR/2024/BATCH8/13).

## REFERENCES

[1]. Abbasi, A., Khojasteh, H., Keihan, A.H. *et al.* (2021). Co-precipitation synthesis of Ag-doped $NiCr_2O_4$ nanoparticles: investigation of structural, optical, magnetic, & photocatalytic properties. *J Mater Sci: Mater Electron* 32, 1413–1426. https://doi.org/10.1007/s10854-020-04913-3.

[2]. Abdel-Latif, I. A., Ismail, A. A., Faisal, M., Ali, A. M., Al-Salmi, A. E., & Al-Hajry, A. (2017). Impact of the Annealing Temperature on Perovskite strontium-doped neodymium manganites nanocomposites & their photocatalytic performances. *Journal of the Taiwan Institute of Chemical Engineers*, *75*, 174–182. https://doi.org/10.1016/j.jtice.2017.03.030

[3]. Abbady, G., Afify, N., Sedky, A., & Hamad, D. (2023). Effect of annealing temperature on structural, optical & magnetic properties of $Cd_{1-x}Mn_xZnO_2$ nanocomposites: An investigation for ferromagnetic. *Ceramics International*, *49*(11), 18042-18054. https://doi.org/10.1016/j.ceramint.2023.02.172

[4]. Adak, M. K., Mondal, D., Mahato, U., Basak, H. K., M&al, S., Das, A., Chakraborty, B., & Dhak, D. (2023). Nanoarchitectonics of zirconium modified $ZnTiO_3$ for photo & electro-catalysts in dye degradation & water splitting applications. *International Journal of Hydrogen Energy*, *48*(100), 39910–39929. https://doi.org/10.1016/j.ijhydene.2023.08.211

[5]. Ahmed, B., Tahir, M. B., Ali, A., & Sagir, M. (2024). First-principles screening of structural, electronic, optical & elastic properties of Cu-based hydrides-perovskites $XCuH_3$ (X=Ca & Sr) for hydrogen storage applications. *International Journal of Hydrogen Energy*, *54*, 1001–1007. https://doi.org/10.1016/j.ijhydene.2023.11.239.

[6]. Ahmed, G., Mohamed, W., Hasaneen, M., Ali, H., & Ibrahim, E. (2023). Optical, Structural, Electrical & Photocatalytic properties of aluminium-doped zinc oxide nanostructures . *Optical Materials*, *140*, 113880. https://doi.org/10. 1016/j. optmat. 2023.113880.

[7]. Akbar, N., Pang, Q., Lu, Y., Jing, Y., Singh, M., Wang, J., Zhu, B., Wang, F., & Yun, S. (2025). Synergistic proton conduction via Ca-vacancy coupled with Li+-bridge in $Ca_5(PO_4)_3OH$. *Communications Materials*, *6*(1). https://doi.org/10.1038/S43246-024-00719-6.

[8]. Amith, S. L., Radhakrishnan, K., & Gurunathan, K. (2024). Utilising e-waste: Development of a room temperature ammonia sensing device featuring highly crystalline GdInO3 nanoballs on surface-active g-$C_3N_4$ Nanosheets. *Journal of Alloys & Compounds*, *1005*, 175930. https://doi.org/10.1016/J.JALLCOM.2024.175930.

[9]. Assar, S.T., Asal, N.A., Moharram, B.M. *et al.* Investigation of structural, elastic, thermal, magnetic, optical, & photocatalytic properties of nanosized Mg-Mn-Li ferrites. *J Sol-Gel Sci Technol* 111, 850–877 (2024). https://doi.org/10.1007/s10971-024-06456-z

[10]. Astuti, Y., Listyani, B. M., Suyati, L., & Darmawan, A. (2021). *Bismuth Oxide Prepared by Sol-Gel Method : Variation of Physicochemical Characteristics & Photocatalytic Activity Due to Difference in Calcination Temperature*. *21*(1), 108–117. https://doi.org/10.22146/ijc.53144

[11]. Bellakki, M. B., Das, J., & Manivannan, V. (2010). Synthesis & Measurement of Structural & M-properties *of* $La_{1-x}Cd_xCoO_3$ *Perovskite Ceramic Oxides*. *3*, 319–325. https://doi.org/10.1007/s10832-009-9576-9.

[12]. Bouazizi, M.L., Hcini, S., Khirouni, K. *et al.* Annealing Temperature Effects on Structural, Magnetic, & Optoelectronic Properties of Mixed $Ni_{0.6}Mg_{0.2}Co_{0.2}FeCrO_4$ Ferrites. *J. Electron. Mater.* **52**, 2878–2893 (2023). https://doi.org/10.1007/s11664-023-10254-8

[13]. Brontowiyono, W., AbdulHussein, W.A., Smaisim, G.F. *et al.* Annealing Temperature Effect on Structural, Magnetic Properties & Methyl Green Degradation of $Fe_2O_3$ Nanostructures. *Arab J Sci Eng* 48, 375–382 (2023). https://doi.org/10.1007/s13369-022-07118-4.

[14]. Chaudhari, G. N., Jagtap, S. V., Gedam, N. N., Pawar, M. J., & Sangawar, V. S. (2009). Sol-gel synthesised semiconducting $LaCo_{0.8}Fe_{0.2}O_3$-based powder for thick film $NH_3$ gas sensor. *Talanta*, *78*(3), 1136–1140. https://doi.org/10.1016/j.talanta.2009.01.030.

[15]. Chauhan, L., Kumar, S., Sreenivas, K., & Shukla, A. (2021). Variable range hopping & modulus relaxation in $NiFe_2O_4$ ceramics. *Materials Chemistry & Physics*, *259*, 124135. https://doi.org/10.1016/j.matchemphys.2020.124135.

[16]. Dippong, T., Levei, E., Lengauer, C. L., Daniel, A., Toloman, D., & Cadar, O. (2020). Investigation of thermal, structural, morphological & photocatalytic properties of $Cu_xCo_{1-x}Fe_2O_4$ ($0 \leq x \leq 1$) nanoparticles embedded in SiO2 matrix. *Materials Characterisation*, *163*, 110268. https://doi.org/10.1016/j.matchar.2020.110268

[17]. Dziazko, O., Nedilko, S., Zaslavsky, O., & Kulichenko, V. (2022). *PHYSICS & CHEMISTRY OF SOLID STATE Synthesis & Properties of Polycharge Phases in the System La-Li-M-Co-O ( M = Ca , Sr , Ba )*. *3*(3), 435–442. https://doi.org/10.15330/pcss.23.3.435-442.

[18]. Goel, P., Sundriyal, S., Shrivastav, V., Mishra, S., Dubal, D. P., Kim, K. H., & Deep, A. (2021). Perovskite materials as superior & powerful platforms for energy conversion & storage applications. *Nano Energy*, *80*. https://doi.org/10.1016/j.nanoen.2020.105552.

[19]. Glinskaya, A., Petrov, G., Vialikanava, I., & Romanovski, V. (2023). Crystal Structure, Magnetic & Photocatalytic Properties of Solid Solutions $Bi_{2-x}La_xFe_4O_9$ (x=0.05, 0.1). *ChemistrySelect*, *8*(8), 2–7. https://doi.org/10.1002/slct.202204285.

[20]. Göktaş, S., & Şahin, G. (2025). Impact of different Cu sources on the structure, surface morphology, optical & photocatalytic characteristics of sol-gel derived CuO thin films. *Türk Doğa ve Fen Dergisi*, *14*(1), 13–20. https://doi.org/10.46810/tdfd.1531667

[21]. Gul, S., Yousuf, M. A., Anwar, A., Warsi, M. F., Agboola, P. O., Shakir, I., & Shahid, M. (2020). Al-substituted zinc spinel ferrite nanoparticles: Preparation & evaluation of structural, electrical, magnetic & photocatalytic properties. *Ceramics International*, *46*(9), 14195–14205. https://doi.org/10.1016/j.ceramint.2020.02.228.

[22]. Hoghoghifard, S., & Moradi, M. (2022). Influence of annealing temperature on structural, magnetic, & dielectric properties of $NiFe_2O_4$ nanorods synthesised by a simple hydrothermal method. *Ceramics International*, *48*(12), 17768-17775. https://doi.org/10.1016/j.ceramint.2022.03.047

[23]. Hussain, S., Javed, M. S., Ullah, N., Shaheen, A., Aslam, N., Ashraf, I., Abbas, Y., Wang, M., Liu, G., & Qiao, G. (2019). Unique hierarchical mesoporous $LaCrO_3$ perovskite oxides for highly efficient electrochemical energy storage applications. *Ceramics International*, *45*(12), 15164–15170. https://doi.org/10.1016/j.ceramint.2019.04.258.

[24]. Ismail, S. A., Saliba, V., Lopez Bernal, J., Ramsay, M. E., & Ladhani, S. N. (2021). SARS-CoV-2 infection & transmission in educational settings: a prospective, cross-sectional analysis of infection clusters & outbreaks in Engl&. *The Lancet Infectious Diseases*, *21*(3), 344–353. https://doi.org/10.1016/S1473-3099(20)30882-3.

[25]. Jacinto, M.J., Ferreira, L.F. & Silva, V.C. Magnetic materials for photocatalytic applications—a review. *J Sol-Gel Sci Technol* **96**, 1–14 (2020). https://doi.org/10.1007/s10971-020-05333-9

[26]. Keerthana, S., Mounasamy, V., & Ponp&ian, N. (2024). Perovskites (ABO3) & their prospects for gas sensor application. *Complex & Composite Metal Oxides for Gas, VOC & Humidity Sensors, Volume 2: Technology & New Trends*, 355–383. https://doi.org/10.1016/B978-0-323-95476-1.00004-6.

[27] Baig, N., Kammakakam, I. and Falath, W., 2021. Nanomaterials: A review of synthesis methods, properties, recent progress, and challenges. *Materials advances*, *2*(6), pp.1821-1871.

[28]. Sreenu K, Prasad NV, Kumar GS, Vithal M, Prasad G. Synthesis and Dielectric Properties of Novel $BaBi_xTi_{1-x}O_{3-\delta}$ Ceramics. Ferroelectrics. 2011 Jan 1;413(1):357-70

[29] Kumar M, Srikanth S, Ravikumar B, Alex TC, Das SK. Synthesis of pure and Sr-doped $LaGaO_3$, $LaFeO_3$ and $LaCoO_3$ and Sr, Mg-doped $LaGaO_3$ for ITSOFC application using different wet chemical routes. Materials Chemistry and Physics. 2009 Feb 15;113(2-3):803-15.

[30] Bi D, Xu Y. Improved photocatalytic activity of $WO_3$ through clustered $Fe_2O_3$ for organic degradation in the presence of $H_2O_2$. Langmuir. 2011 Aug 2;27(15):9359-66.

[31]. Kombaiah, K., Vijaya, J. J., Kennedy, L. J., Bououdina, M., & Al-Najar, B. (2018). Conventional & microwave combustion synthesis of optomagnetic $CuFe_2O_4$ nanoparticles for hyperthermia studies. *Journal of Physics & Chemistry of Solids*, *115*, 162-171. https://doi.org/10.1016/j.jpcs.2017.12.024.

[32]. Ilves, V., Gaviko, V., Murzakaev, A., Sokovnin, S., Svetlova, O., Zuev, M., & Uimin, M. (2024). Effect of air annealing on structural, textural, thermal, magnetic & photocatalytic properties of Ag-doped mesoporous amorphous crystalline nanopowders $Bi_2O_3$. *Nano-Structures & Nano-Objects*, *39*, 101319. https://doi.org/10.1016/j.nanoso.2024.101319

[33]. Lomanova, N. A., Osipov, A. V., Ugolkov, V. L., Kenges, K. M., & Yastrebov, S. G. (2025). Facile solution combustion synthesis of $BiFeO_3$ nanopowder with improved magnetic & photocatalytic characteristics. *Inorganic Chemistry Communications*, *178*, 114591. https://doi.org/10.1016/J.INOCHE.2025.114591.

[34].Qi Dai, Qi-Qi Liang, Tian-Yu Tang, Hua-Xu Gao, Shi-Quan Wu, Yan-Lin Tang (2024). Physical Properties of Novel double perovskite oxides $Ba_2XSbO_6$(X = P, As) by first-Principal calculations. *Journal of Chemical Physics*, 586, (1), 112392

[35] Vandana, C.S. & Rudramadevi, B.H. (2020). Structural, magnetic and dielectric properties of cobalt doped $GdFeO_3$ orthoferrites. *Materials Research Express,* 6(12):126126.

[36] Junploy, P., Thongtem, S. and Thongtem, T., 2013. Photoabsorption and photocatalysis of SrSnO3 produced by a cyclic microwave radiation. *Superlattices and microstructures*, *57*, 1-10.

[37] Lee, M.J., Jun, J.H., Jung, J.S., Kim, Y.R. and Lee, S.H., 2005. Catalytic activities of perovskite-type $LaBO_3$ (B= Fe, Co, Ni) oxides for partial oxidation of methane. *Bulletin of the Korean Chemical Society*, *26*(10),1591-1596.

[38] Xiong, G., Zhi, Z.L., Yang, X., Lu, L. and Wang, X., 1997. Characterization of perovskite-type $LaCoO_3$ nanocrystals prepared by a stearic acid sol--gel process. *Journal of materials science letters*, *16*(13), pp.1064-1068.

[39] Barbero, B.P., Gamboa, J.A. and Cadús, L.E., 2006. Synthesis and characterisation of $La_{1-x}Ca_xFeO_3$ perovskite-type oxide catalysts for total oxidation of volatile organic compounds. *Applied Catalysis B: Environmental*, *65*(1-2), pp.21-30.

[40] Zhang, Y., Yang, J., Xu, J., Gao, Q. and Hong, Z., 2012. Controllable synthesis of hexagonal and orthorhombic $YFeO_3$ and their visible-light photocatalytic activities. *Materials Letters*, *81*, pp.1-4.

[41]. Reddy, N.M., Koth&an, D., V, P.R. *et al.* Collating the structural, vibrational, & photocatalysis properties of $LaFeO_3$ rare-earth orthoferrite nanoparticles synthesised by the sol-gel method. *J Sol-Gel Sci Technol* 113, 322–330 (2025). https://doi.org/10.1007/s10971-024-06602-7

[42]. Roostaei, S., Ansarinejad, H., Dawi, E. A., Alsultany, F. H., & Khalaf, S. (2025). *Sol – gel auto - combustion synthesis of a novel ternary magnetic - recyclable - $ZnFe_2O_4/ZnO/CeO_2$ nano - photocatalyst for highly efficient visible - light - induced degradation of organic contaminants*.

[43]. Shah, M. A. K. Y., Tayyab, Z., Rauf, S., Yousaf, M., Mushtaq, N., Imran, M. A., Lund, P. D., Asghar, M. I., & Zhu, B. (2021). Interface engineering of bi-layer semiconductor $SrCoSnO_{3-\delta}$-$CeO_{2-\delta}$ heterojunction electrolyte for boosting the electrochemical performance of low-temperature ceramic fuel cell. *International Journal of Hydrogen Energy*, *46*(68), 33969–33977. https://doi.org/10.1016/j.ijhydene.2021.07.204.

[44]. Sundaram, G. A., Muniy&i, G. Raj, Ethiraj, J., Parimelazhagan, V., & Kumar, A. S. K. (2024). Introduction & Advancements in Room-Temperature Ferromagnetic Metal Oxide Semiconductors for Enhanced Photocatalytic Performance. In *ChemEngineering* (Vol. 8, Issue 2). https://doi.org/10.3390/chemengineering8020036

[45]. Zhang, M., Feng, C., Zhang, W., Luan, X., Jiang, J., & Li, L. (2013). Synthesis of Bismuth Nanoparticles by a Simple One-Step Solvothermal Synthesis of Bismuth Nanoparticles by a Simple One-Step Solvothermal Reduction Route. *Applied Mechanics and Materials, September 2013*, 1–6. https://doi.org/10.4028/www.scientific.net/AMM.423-426.155